RAM
ROBOTICS
AND
MECHATRONICS

Generating high frame rate MRI images using a surrogate signal

K. (Kirelloss) Shokry

MSc Report

Committee:
Dr.ir. M. Abayazid
H. Naghibi Beidokhti, MSc
Dr. B. Sirmaçek
Dr.ir. B. ten Haken
Dr.ir. F. van der Heijden

UNIVERSITY OF TWENTE.

MIRA CTIT
BIOMEDICAL TECHNOLOGY
AND TECHNICAL MEDICINE

Preface

In this thesis, I present two solutions for increasing the efficiency of percutaneous minimally invasive procedures and enabling real-time imaging. The topic combines my interest in image processing, computer vision and machine learning. The presented work was carried out using two programming languages Matlab and Julia. Also, it included some experiments using ultrasound, skin markers and a phantom for validating the suggested approaches.

Also, I would like to thank a lot of people for helping me and facilitating this presented work either on the academic or the personal level. Firstly, I would like to thank my supervisors: Dr Momen , Dr Hamid and Dr Beril for encouraging me and helping me develop my skills. Also, I am so grateful for their great efforts in helping me during my illness for one and half month during critical part of my work. Secondly, I would like to thank Prof Molenkamp and Prof Kokkeler for all the skills they helped me develop and their continuous support on the personal level. Also, I would like to thank my friends: Mohammad Elhawary, Rosie, Mohab, Megumi, Shiho, Joshua, Miri, Evelina, Dink and Juan for sharing a lot of great moments, which made me feel home in Netherlands. Finally, I am so thankful and proud of my family; my parents and my two sisters, who are always there for me and give a great meaning for my life. I would like to end this part with a quote which always inspires me "There is nothing impossible to him who will try".

Kirelloss,
September, 2018

High Frame Rate Synthetic MR Images for the Liver using a Surrogate Signal and Machine Learning
A Supervised Learning Approach

Kirelloss Shokry, kirellossshokrysamirshokry@student.utwente.nl, s1818694 , Embedded Systems

Abstract— MR images are needed in many percutaneous minimally invasive procedures in the liver. However, the acquisition of MRI happens at low frequency, which doesn't enable real-time imaging under respiratory induced motion in the liver. One main contribution of this study is that it presents a new technique for generating synthetic MR images that have contrast and spatial resolution higher than the acquired ones. The new approach depends on respiratory motion estimation in the liver using a surrogate signal. Synthetic MR images are predicted at the same high frequency of the surrogate signal. Also, this study presents a new machine learning algorithm for predicting the x-y pixel coordinates of small targets with very high accuracy and frequency without generating full images. The strength of this algorithm is that it tries to find the exact non-linear function between the surrogate signal and the position of targets in the MR image if it exists. Otherwise, the algorithm tries to capture the correlation between them as close as possible. The correctness of the first technique was evaluated by comparing the locations of liver features and the contours of the liver in synthetic images to their corresponding acquired ones. The mean error ranged between 0.659 pixel (1.3839 mm) and 1.2154 pixels (2.55 mm). The average blurriness of synthetic images was 0.3305, while that of corresponding acquired ones was 0.3306. The average entropy of synthetic images was 6.5631, while that of corresponding acquired ones was 6.5248. The mean error of the second technique was evaluated by comparing the predicted positions of targets to their real positions. The mean error ranged between 0.9859 pixel and 1.0034 pixels after training the algorithm by 50% of the acquired data. The mean error decreased to range between 0.8669 pixel and 0.8758 pixel after training the algorithm by 75% of the acquired images. The algorithm was tested every time by the last 25% of the obtained data. Both techniques were evaluated by open source data, previously carried out experiments and experiments carried out on a phantom.

Index Terms— **3D vision, Image Processing, Ultra-Sound, Respiratory Induced Motion, Surrogate Signal, MRI, Supervised Machine Learning.**

I. INTRODUCTION

A. Respiratory Induced Motion

Liver Cancer is the second main cause of cancer deaths worldwide [2]. 70% of cancer deaths happen in developing countries because of the lack of proper diagnosis and treatment. According to the World Health Organization (WHO), 30%-50% of cancer patients could recover if cancer is diagnosed early and treated properly [3]. Percutaneous image-guided minimally invasive procedures are widely performed during cancer treatment in the liver. They are used for many purposes such as: biopsy, fluid collection drainages and tumor ablation [4]. Percutaneous minimally invasive procedures offer many advantages such as: lower complication rates, shorter recovery time, shorter hospital stays and less expenses [5]. However, hepatic motion due to respiration is a main obstacle for precise percutaneous instrument insertion [5] [9].

Respiration leads to liver motion in different directions mainly: superior-inferior (SI) and anterior-posterior directions (AP). Also, it leads to liver deformation as the liver is a non-rigid body [5]. The respiratory induced liver motion is more dominant in the superior-inferior direction, where it could range from 8 mm to 25 mm [10] [11]. The average frequency of human breathing is between 12-15 breathes per minute [12]. Therefore, if the imaging modality doesn't provide high update rate or the respiratory induced motion is not compensated, this would result in motion artifacts in the images and inaccurate targeting for lesions [13]. Some of the consequences of inaccurate targeting are: damage of healthy cells during needle insertion, misdiagnosis in case of biopsy and insufficient treatment in case of ablation [4].

B. Respiratory Motion Compensation

Different imaging modalities are used in image guided interventions such as: magnetic resonance imaging (MRI), ultrasound (US), fluoroscopy and computed tomography (CT) [4]. MRI is preferred for soft tissue organs such as

the liver. That is because it results in high quality non-invasive images with high spatial resolution and contrast. This enables the detection of small lesions [6] [7]. Getting high quality and high frequency images are contradicting properties. For instance, MRI results in high quality images but obtained with low frequency, while the opposite is true for ultrasound [7].

Therefore, many approaches have been suggested in literature for compensating respiratory induced motion in the liver. These approaches could be divided into either active or passive approaches [4]. The active approach is breath holding. The breath should be held at the same respiratory phase during imaging and instruments insertion. Statistics showed that 10-15% couldn't hold their breath for a sufficient time [14]. On the other hand, passive approaches compensate for respiratory induced motion without breath holding. One example for a passive approach is "respiratory gating". This technique allows operating on the tissue only at identical points in the respiratory cycle. End of exhalation is usually chosen as it represents the longest natural pause [5]. The disadvantage of this technique is that features in the liver don't occupy the same position at identical lung volumes [16]. Another example for a passive approach is "Modelling", where a model is created for predicting the liver motion from previously acquired images [5]. The limitation of this technique is that the motion of the liver differs from one respiration cycle to another. One main passive approach is inferring the position of a target in the liver by combining an imaging modality with high resolution like MRI and a surrogate signal that can be obtained with high temporal frequency. The surrogate signal should have very high correlation with the imaged target [17]. The components of this technique are as follows: target motion data, surrogate data, motion model, fitting method and target motion estimate [15]. The "Motion Model" is developed between the surrogate signal and the target motion based on a supervised machine learning trained by target data and surrogate data obtained simultaneously. Depending on this model and only the provided surrogate signal, the target motion could be estimated at the same high frequency of the surrogate signal.

C. Surrogate Signals

Different surrogate signals have been proposed in literature such as: spirometer, respiratory bellows, reference needle, skin markers, single element transducer etc. [4] [7] [15]. Spirometers measure the air flow out and into the lungs. They have the advantages of high correlation with respiration motion and they provide simple one-dimensional signal. The main disadvantages are that they are prone to drift due to air leakage and cause

discomfort to patients [15]. The respiratory bellow is an air-filled bag that's wrapped around the patient's thorax or abdomen to measure its motion by measuring the air flow out and inside the bag. It has the same advantages and disadvantages of the spirometer. Also, its placement restricts the operating area of the patient [15]. A reference needle could be inserted in the liver and its motion data could be used as a surrogate, guiding the insertion of subsequent needles [4]. However, this adds the challenge of proper placement of the needle close to the target. The usage of optically tracked skin markers has been suggested and used as a surrogate signal by different studies [15] [18] [19] [20] [21]. However, the liver doesn't have any fixed relationship with the skin surface or surrounding organs as reported by [22]. An MRI compatible single element ultrasound transducer could also be used as a surrogate signal. A single element transducer has the advantages of: high correlation with liver and respiration motion, no restriction for the operating area for MR, ultrasound data acquisition happens in parallel and synchronized with MRI acquisition and it doesn't reduce the time needed for MRI acquisition [7]. The main disadvantage of using ultrasound as a surrogate signal is that the setup is complex and expensive. Preiswerk et al. suggested that the field of the ultrasound sensor shouldn't be focused for the received signal to act as a unique signature for the arrangement of the organs at different points in time [7].

D. Contribution

The study presents a new technique for respiratory motion compensation using the passive approach of a surrogate signal. The imaging modality used is MR. This technique generates synthetic MR images of the liver at the same high frequency of the surrogate signal. One main contribution of this paper is that synthetic images generated by this technique have spatial resolution and contrast better than the real acquired images. Having high frequency MR images with high contrast and spatial resolution is very beneficial for tracking and targeting small lesions in the liver under respiratory induced motion with very high accuracy. This in turn allows accurate percutaneous instruments insertion even for very critical targets. This algorithm was tested by using two different surrogate signals. The first is skin markers and the second is ultrasound.

Then, the study presents a new machine learning algorithm for predicting the x-y pixel coordinates of small targets inside the MR image of the liver with very high accuracy and frequency without generating synthetic images. This algorithm has the ability to conclude the exact non-linear mathematical function between the

surrogate signal and the position of targets in the MR image of the liver, if it exists, not just fitting a pre-chosen function to the data. If no exact mathematical function exists, it tries to capture the correlation between the surrogate signal and the targets as close as possible. The new learning algorithm is named "evolving function" as the function has the ability to change and improve itself over time as long as more data is provided to give a better modelling of the previously mentioned mathematical relation or correlation.

Also, this study presents a phantom experiment that was carried outside the MR. Surrogates used in the experiment were skin markers and ultrasound. More than one surrogate signal was used to evaluate whether it is important to use a precise surrogate with a complex and expensive setup like ultrasound or it is just sufficient to use a cheap one with less correlation to the target motion like skin markers to get results with accepted accuracy.

II. BACKGROUND

A. *MRI Formation*

Before explaining the new idea, the process of MRI formation is explained as this would give a better understanding of the new technique. MR image is a display of the RF signals received from the tissues during imaging. Bright points in the image represent tissues emitting high intensity radio frequency (RF) signals and vice versa. The source of these RF signals is the magnetization applied to tissues during MR scanning [23]. The magnetization of tissues takes place due to the presence of hydrogen atoms in tissues; whose nuclei consist of a single proton. These protons have a magnetic property called "magnetic moment". When protons are placed in a strong magnetic field, some of them align in the same direction of the magnetic field, which leads to the magnetization of the tissues and in turn RF signals emission. An imaged slice of tissues is divided into rows and columns of individual volume elements called voxels, where each voxel corresponds to a pixel in the image. One MR image acquisition consists of an acquisition cycle of period *TR*, which is repeated *n* times to form the image [24]. Every acquisition cycle, magnetic field gradients are turned on and off across the dimensions of the imaged tissues. In every cycle, frequency-encoding gradient is turned on during the echo event when RF signals are emitted by the tissues. This gradient is applied along one of the two dimensions of the imaged slice, where magnetic field is increased along that dimension as shown in Figure 1. This leads to voxels resonating at different frequencies along that dimension,

where voxels present at higher magnetic field strength emit RF signals with higher frequency and vice versa.
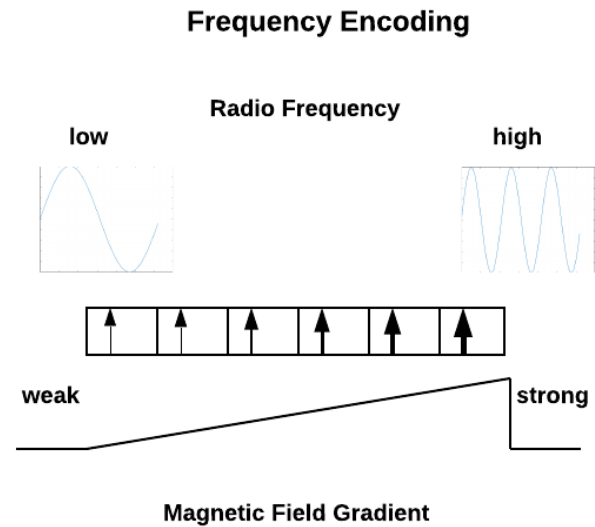

Figure 1: Frequency-encoding gradient in MRI.
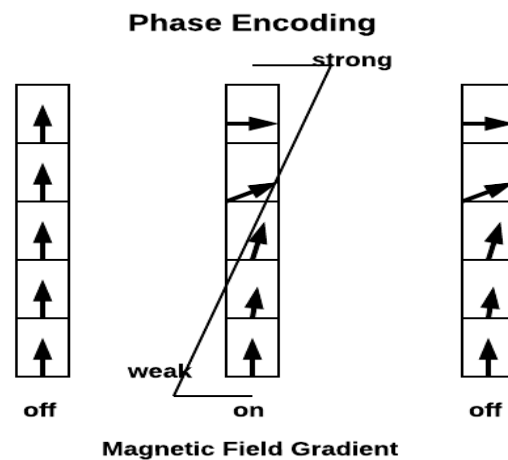

Figure 2: Phase-encoding gradient in MRI.

Also, every acquisition cycle, phase-encoding gradient is turned on for a short period by increasing the magnetic field along the other dimension of the imaged slice as shown in Figure 2. This causes magnetization from voxel to voxel along that dimension to get out of step, which creates a phase difference between RF signals emitted by these voxels. The strength of the phase-encoding gradient is changed slightly from one acquisition cycle to another [23]. Due to the effect of these two gradients, voxels in the imaged slice emit RF signals which are different in both phase and frequency. All of these signals are emitted at the same time and collected by the imaging device at

echo time as a single composite signal. Every acquisition cycle, this composite signal is digitized and stored in computer memory in a configuration called k space. One or more rows in the k space matrix are filled every acquisition cycle as shown in Figure 3 [23]. The k space matrix is the 2D Fourier transform of the MR image. It is in spatial frequency and is conjugate symmetric. The total acquisition time of one MR image is:

$$T = TR \; x \; NY \; / \; (Nechoes \; x \; R) \qquad [1]$$

, where N_Y is the size of the image matrix, N_{echoes} is the number of k space lines per TR period and R is the acceleration factor [7]. After the k space matrix is filled, image reconstruction takes place by applying inverse Fourier transform.
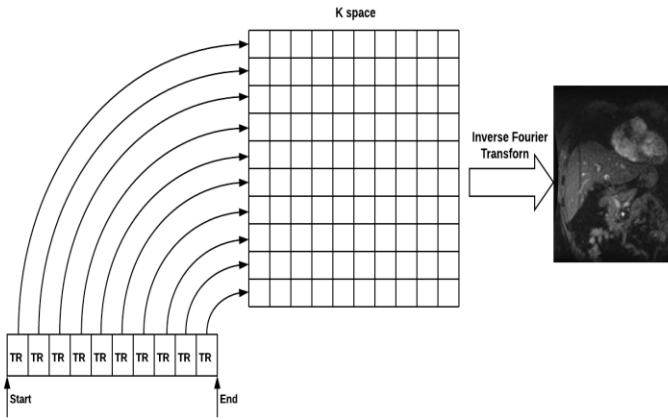

Figure 3: K space matrix filling and image reconstruction.

B. Related Work

The first approach represented by this paper in is an improvement of the idea presented by Preiswerk et al. in [7]. This study presented an approach for generating high frame rate MR images using ultrasound as a surrogate signal. In this approach, the acquisition of surrogate signal readings is triggered by the repetition cycle TR, where a surrogate signal reading is acquired every TR. Since, one image acquisition takes $n * TR$ time units. Therefore, every image corresponds to the acquisition of n surrogate signal readings, where the last of these surrogate signal readings corresponds to the acquisition of the k space center of the image. D represents all acquired data. Each entry in D is a pair {I_T, U_T}, where I_T represents the image acquired at time points T and U_T represents the n surrogate signal readings corresponding to this image. The approach presented in this paper is based on a Bayesian learning algorithm. Each time a new surrogate signal reading is acquired at time t, it is combined with $n - 1$ readings acquired before it to form a signal U_t . U_t is used to predict a synthetic MR image I_t

whose k space center corresponds to the acquisition of this new surrogate reading, depending on past acquired data D as follows:

$$E[It \;|Ut, D] = \int It \; p(It \;|Ut, D) dIt = \frac{\int It \; p(It, Ut \;|\; D) \; dIt}{p(Ut \;|D)} \qquad [2]$$

$$\int I \; t \; p(It, Ut \;|\; D) \; dIt \; \approx \; \frac{1}{NT}\sum_i Ii \; N(Ut; Ui, \Sigma) \qquad [3]$$

$$p(Ut \;|D) \approx \frac{1}{NT}\sum_i \; N(Ut; Ui, \Sigma) \qquad [4]$$

$$E[It \;|Ut, D] \; \approx \; \frac{\sum_i Ii \; N(Ut; Ui, \Sigma)}{\sum_i \; N(Ut; Ui, \Sigma)} \qquad [5]$$

, where $p(It, Ut \;|\; D)$ is the joint density of the MR image I_t and signal U_t. N_T is the number of all acquired MR images so far. i loops over all entries in D, where {I_i, U_i} represents a single pair. $N(Ut; Ui, \Sigma)$ is a Gaussian kernel that measures the degree of closeness between U_t and each U_i in D. Therefore, every predicted image I_t is a summation of weighted acquired images so far divided by the sum of all weights. The weight assigned to each image I_i depends on the degree of closeness between U_t and U_i.

III. MATERIALS AND METHODS

A. New Approach for Synthetic MRI Generation

A.1 Learning Algorithm

Let, *T*: The collection of time points at which a single MR image is Formed.

  I_T: MR image acquired at time points T.

  TR: Period of the acquisition cycle.

  n: Number of acquisition cycles required to form a single MRI.

  N_{TR}: number of k space lines acquired every *TR* period

As it has been explained, every MR image I_T consists of a set of individual k space lines, where a number N_{TR} rows of the k space are collected every repetition interval *TR*. The collection of the reading of a surrogate signal in this paper was triggered by the repetition time *TR*. One MR corresponds to the collection of *n* readings of the surrogate signal. Therefore, the frequency of collecting a reading of the surrogate signal is *n* times higher than that of MRI acquisition as shown in Figure 4. The learning algorithm introduced in this subsection generates synthetic images at the same high frequency of the surrogate signal, which is *n* times higher than the acquisition frequency. The average human breathes are between 12-15 breathes per minute. Therefore, one respiratory cycle takes between 4-5 seconds. one MR image acquisition could take up to 1 second [15]. This

means that the duration of one MR image acquisition could take up to the quarter of a respiration cycle. Each
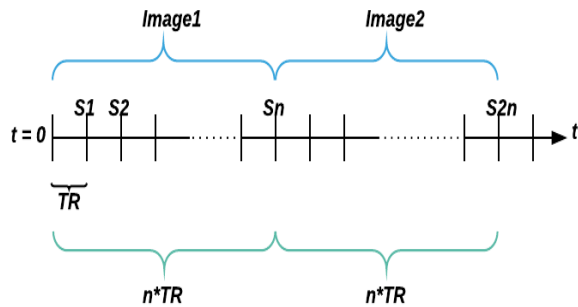

Figure 4: Surrogate signal acquisition, which is acquired with frequency n times higher than that of MR images. S_x refers to surrogate signal reading obtained at time x*TR, where x is a positive integer.

MR image is not formed at one point in time, where the last signals in the k space are collected at a time $(n-1) * TR$ time units later than the first ones in the k space. This in turn indicates that the phase difference between the collection of the last entry in the k space and the first one of the same image could reach up to the quarter of a respiration cycle, which is a huge shift. Since, the liver is not a stationary organ, but it moves in different orientations due to respiration. Therefore, the entries of the k space of one MR image represent the liver in different positions, not in a single position. This leads to a reduced spatial resolution and contrast in the acquired image. Although considering each acquired MR image as a single unit will result in generating predicted images at the same frequency of the surrogate signal, which is $1/TR$ in this paper, these images will be predicted as if each has been acquired over $n * TR$ time units, resulting in the same phase shift of $(n-1) * TR$ time units between the last and first entries of the k space of each predicted image as shown in Figure 5. So, any learning algorithm that considers each acquired MR image as a single unit will result in predicted images with poor spatial resolution and contrast. An example of these algorithms is the algorithm introduced in [7], which resulted in blurred synthetic images with contrast worse than the real acquired ones. This study presents a new technique that generates synthetic MR images, where all the entries of the k space of each represent the same respiratory phase and same position of the liver. It no longer considers an acquired MR image as a single unit. However, each MR image is disassembled into n entries of the k space forming it, where each of these entries was acquired in a different acquisition cycle.
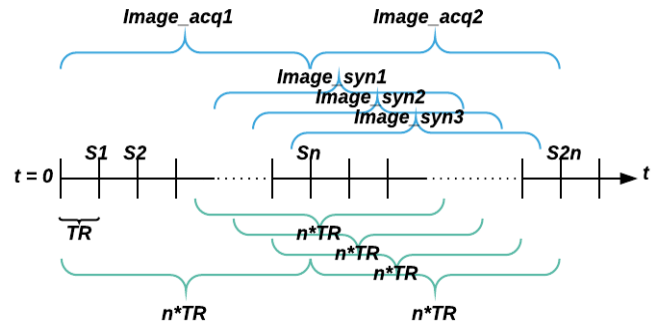

Figure 5: Synthetic images generated considering each acquired MR image as a single unit. They are generated at high frequency of 1/TR. However, they are predicted as if they have been acquired for n*TR time units. "Image_syn" refers to synthetic images, while "Image_acq" refers to acquired ones.

The smallest unit used to build predictions from is N_{TR}, which represents the number of k space lines acquired every acquisition time TR. This algorithm creates a number $\lfloor n/2 \rfloor + 1$ of databases, which is almost equal to the half the number of acquisition cycles per acquired image. Every database consists of a number of N_{TR} k space lines equals to double the number of acquired images and corresponding surrogate signals acquired simultaneously with each of these N_{TR} k space lines . Each database has entries double the number of acquired images because the k space matrix is conjugate symmetric as shown in Figure 6. The exception is that the number of entries of the last database is exactly equal to the number of acquired images as it consists of the N_{TR} k space rows representing the k space centers in all acquired images. The first database consists of the first N_{TR} k space rows and the conjugate of the nth N_{TR} k space rows in all acquired images and corresponding acquired surrogate signals to each. The second database consists of the second N_{TR} k space rows and the conjugate of $(nth - 1)$ N_{TR} k space rows in all acquired images and corresponding acquired surrogate signals and so on as shown in Figure 7. The prediction of a new image could only start when every database has at least one entry of N_{TR} k space rows and the corresponding surrogate signal.
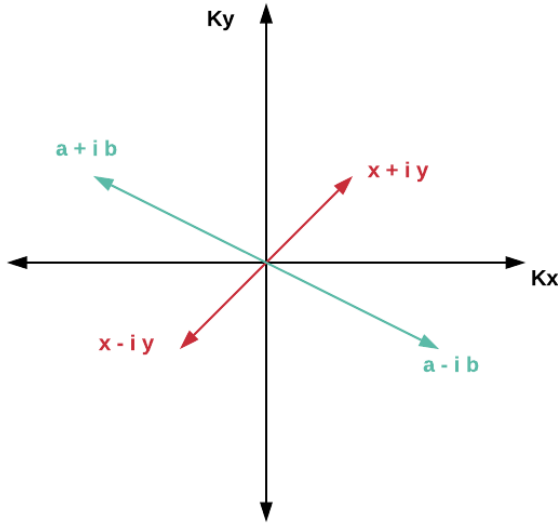
Figure 6: K space matrix is conjugate symmetric, where the imaginary component at opposite K space co-ordinates has the opposite sign.

The advantage of this new algorithm is that all k space lines of the predicted image correspond almost to the same point in respiratory phase and liver position and there is no longer the shift of $(n-1) * TR$ time units between the last and first entries of the k space as it is the case for the acquired images. Also, the property that the k space matrix is conjugate symmetric is preserved. This means that any predicted image using this technique is equivalent to an image fully captured at the same point in time for a duration almost equal to TR time units as shown in Figure 8. This explains why predicted images using this technique have higher spatial resolution and contrast than acquired images corresponding to them as will be shown in "Results" section.
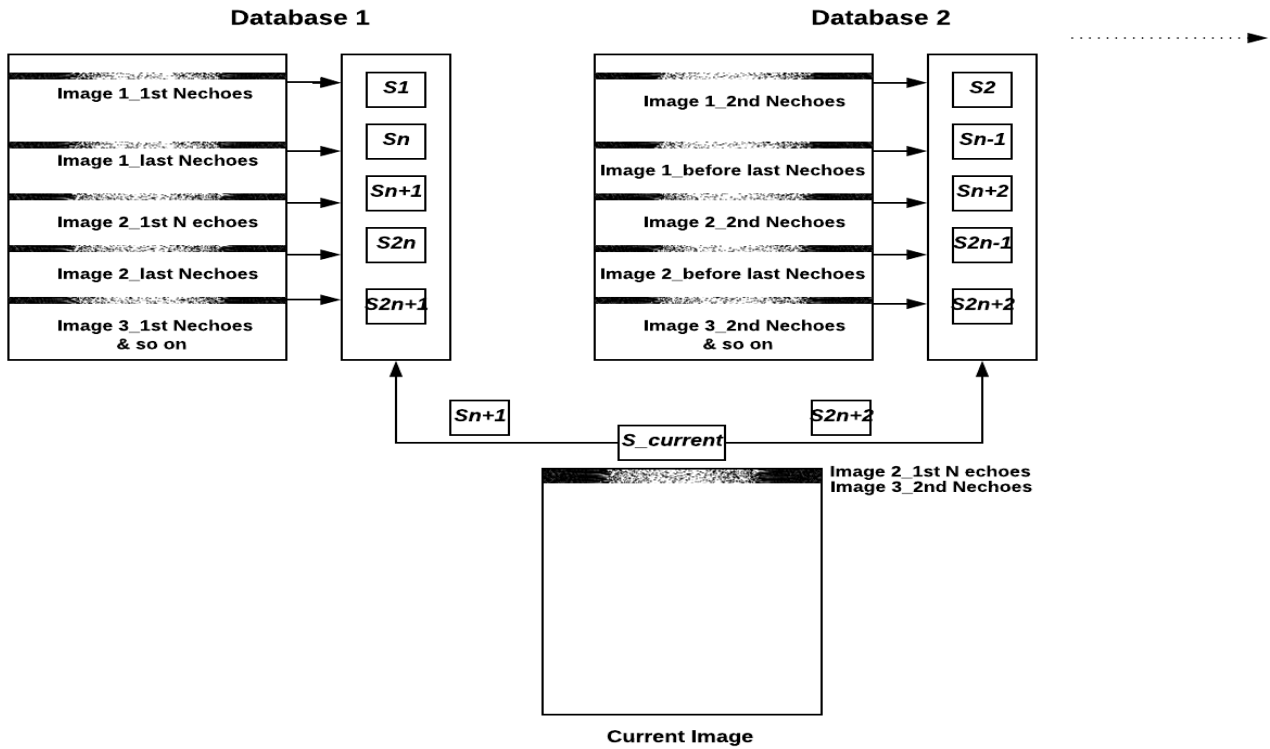
A synthetic image is generated every time a new surrogate signal is obtained. A Gaussian kernel $k\ (S_t,\ S_{xn})$ is used as the learning algorithm in the form of:

$$k\ (S_t,\ S_{xn}) = exp(\ -\frac{1}{2}\ (S_t - S_{xn})^T\ \Sigma^{-1}(S_t - S_{xn})) \qquad [6]$$

, where S_t: represents the newly acquired surrogate signal at time t, S_{xn}: represents the surrogate signal number x in database n, for instance S_{21} represents the second surrogate signal in the first database, Σ is a covariance matrix. When the reading of a new surrogate signal is acquired, the Gaussian kernel is applied to measure the degree of closeness between the newly acquired surrogate and all surrogates in each database. Half of the k space of the predicted image is filled by k space lines from different images in the databases, whose corresponding surrogates are the closest to the newly acquired one. This means that these k space lines correspond to almost the same point in respiratory phase and liver position of the newly acquired surrogate. The $N_{TR}k$ space lines corresponding to the closest surrogate signal to the newly acquired one in the first database are used to fill the first $N_{TR}\ k$ space lines in the predicted image. The $N_{TR}\ k$ space lines corresponding to the closest surrogate signal to the newly acquired one in the second database are used to fill the second $N_{TR}\ k$ space lines in the predicted image and so on as shown in Figure 7. When half of the k space of the predicted image is full, image reconstruction is applied in two steps. Firstly, the second half of the k space matrix is filled as conjugate symmetric from the first half to avoid any asymmetry between the two halves of the k space matrix, which leads to reduced spatial resolution and contrast. Secondly, inverse Fourier transform is applied to transform the image into the 2D space domain.

Figure 7: Newly introduced high frame rate MRI technique explanation. "S_x" refers to the reading of the surrogate signal acquired at time x. For instance, S_n refers to the surrogate signal obtained simultaneously with the last repetition cycle in the acquisition of the first image. S_{n+1} refers to the surrogate signal obtained simultaneously with the acquisition of the first repetition cycle of the 2nd image. "current image" refers to the synthetic image generated simultaneously with the arrival of a new surrogate signal "S_current". "S_{n+1}" is the closest surrogate reading to "S_current" in the first database. "S_{2n+2}" is the closest reading to "S_current" in the second database.

Figure 8: Synthetic images generated by the new technique. They are generated at high frequency of $1/TR$ and as if each has been acquired only in TR time units. "Image_syn" refers to synthetic images, while "Image_acq" refers to acquired ones
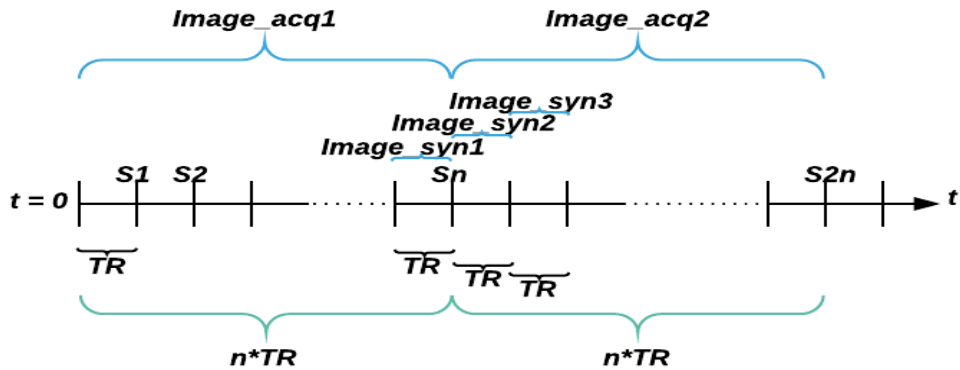
B. "Evolving Function" Machine Learning Algorithm

Another contribution of this study is that it presents a new algorithm for predicting the x-y pixel coordinates of small targets in the MR image with very high accuracy and at the same high frequency of the surrogate signal without generating synthetic images. The strength of the new algorithm is that it doesn't fit a pre-chosen function to the data to generate a mathematical model between the surrogate signal and the position of targets in MR images. However, it tries to capture the exact non-linear function between both of them if it exists. If no exact mathematical relation exists, the generated mathematical model tries to capture the correlation between the surrogate signal and position of targets as precisely as possible. As more data is provided, the algorithm tries to capture the real mathematical relation or the correlation more precisely. That's why it is called "Evolving Function" as the mathematical model evolves over time as long as more data is provided.

B.1 Learning Algorithm:

Let, T: The collection of time points at which a single MR image is formed.

I_T: MR image acquired at time points T.

D_T: Set of surrogate signals time-matching the acquisition of image I_T.

As it was stated before, each MR image consists of a set of individual k space signals, each is acquired every repetition cycle TR and it takes n repetition cycles to form a single image. A surrogate signal reading is obtained every TR. Therefore, n surrogate signal readings correspond to an image acquisition, where the last of these surrogate readings is time-matched with the acquisition of the k space center of the image. Each n surrogate signals corresponding to an image I_T are considered as a single unit in this algorithm named D_T.

The function between targets in the MR image and the surrogate signal could be represented in two ways:

- Equation
- Graphical Representation

This machine learning algorithm tries to find the graphical representation of the exact function between the surrogate data and the targets if it exists or the function modelling the correlation between them otherwise. This graphical representation is in 2D. The x-axis represents the surrogate signal, while the y-axis represents the position of targets in pixels. The steps of developing the "Evolving Function" between the surrogate signal and a certain target in the MR image are as follows. Firstly, the surrogate signal readings corresponding to acquired images are represented on the x-axis. D_T, corresponding to the maximum inhalation or exhalation among all collected sets of data, is chosen as the reference set of surrogate signals, D_{ref}. Since, each reading of the surrogate signal is multi-dimensional, which couldn't be represented on a single axis. Therefore, the readings of the surrogate signal are represented on the x-axis by the degree of their closeness to the reference one. Hence, the range of values represented on the x-axis is from "0" to "1". Large fractions close to "1" on the x-axis refer to readings so close to the reference one, which is represented by "1" on the x-axis, and vice versa. The degree of closeness between readings of the surrogate signal and the reference one is measured using a Gaussian kernel in the form of:

$$k\,(D_T,\,D_{ref}) = exp(\,-\frac{1}{2}\,(D_T - D_{ref})^T\,\Sigma^{-1}(D_T - D_{ref})) \qquad [7]$$

As D_T gets closer to D_{ref}, as the shift between the respiratory phase represented by D_T and that represented by D_{ref} decreases and vice versa. Secondly, the displacement of the target in pixels in all acquired images with respect to its position in the image corresponding to the reference signal D_{ref} is measured using the Euclidian distance and is represented on the y-axis as shown by blue circles in Figure 9.
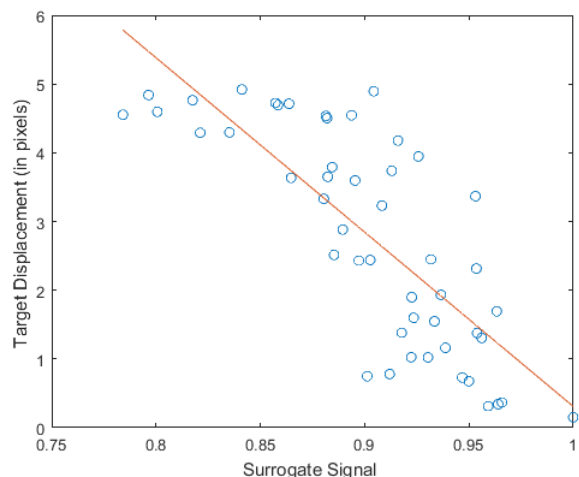

Figure 9: Target displacement in all acquired images compared to the reference one. The red line is a straight line, which is fitted to the data.

So every point in this graph is a pair $(p_x,\,p_y)$. "p_y" is the displacement of the target in pixels in a certain acquired MR image with respect to its position in the reference image. "p_x" is the degree of closeness between the set of readings of the surrogate signal D_T, corresponding to this MR image, and the reference one D_{ref}. It could be observed that there is a correlation between the closeness of the reading of D_T to D_{ref} and the displacement of the

target, where both are inversely proportional. The closer the reading of D_T to D_{ref}, the less displacement of the target and vice versa. Thirdly, noisy data, which results from errors in tracking the target or sudden changes in the respiratory induced motion due to coughing or gasping, is removed. This is achieved by fitting a straight line to the data. This line captures the correlation between the surrogate signal and the position of the target as shown in Figure 9. The error between the values of the y-axis of all acquired points and the values of the y-axis of points on the fitted straight line corresponding to the same reading of the surrogate signal is computed by measuring the absolute distance between them. Acquired points whose y-axis have an absolute distance with respect to the corresponding ones on the fitted line greater than a certain hysteresis value are eliminated as shown in Figure 10. This hysteresis value is chosen here to be 0.6 of the standard deviation of all of the values of target displacement with respect to its reference position.
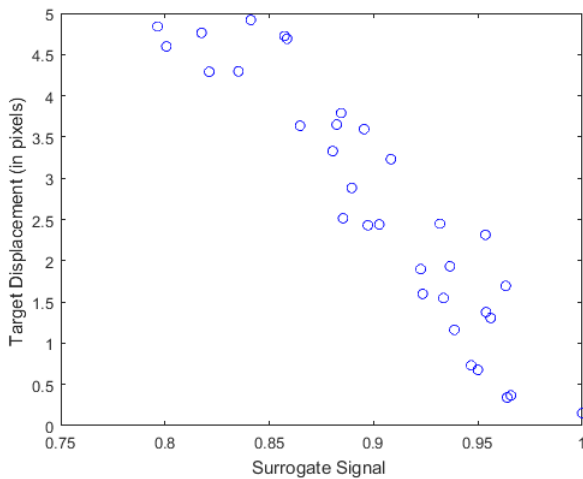

Figure 10: Removal of noisy data from the graph

After this step, only reliable points are preserved. Fourthly, two graphs are created from the reliable data preserved after noise removal to capture the relation between the surrogate signal and the target. The plot in Figure 9 between the displacement of the target and the surrogate signal was developed to find the correlation between the target displacement and the surrogate signal to help in noise removal as shown in Figure 10. However, in this step two graphs are developed between the surrogate signal and the position of the target in pixels in the MR image instead of its displacement compared to the reference one, using only reliable points after noise removal as explained in Figure 10. Every point in the first graph is a pair (p_x, p_y). "p_y" is the column position of the target in a certain acquired MR image in pixels. "p_x" is the ratio between the reading of the surrogate signal D_T,

corresponding to this MR image, and the reference reading D_{ref} as shown by red circles in Figure 11.
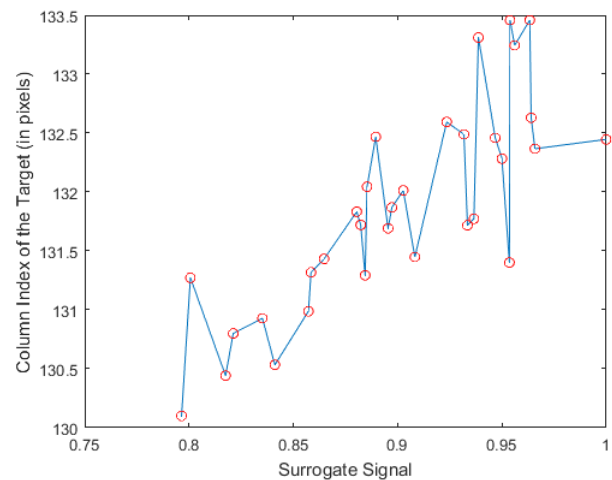

Figure 11: Plot of the column index of the target in different images in pixels and the ratio between D_T, corresponding to each of these images, and D_{ref}.

Every point in the second graph is a pair (p_x, p_y). "p_y" is the row position of the target in a certain acquired MR image in pixels. "p_x" is the ratio between the reading of the surrogate signal D_T, corresponding to this MR image, and the reference reading D_{ref} as shown by red circles in Figure 12.
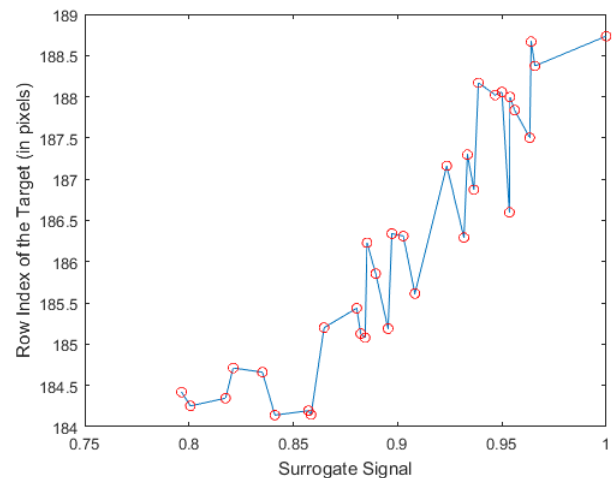

Figure 12: Plot of the row index of the target in different images in pixels and the ratio between D_T, corresponding to each of these images, and D_{ref}.

Finally, linear interpolation is performed in both graphs, where every point is connected to the successive one by a straight line as shown in Figures 11 and 12. As more images are acquired, more reliable points are acquired by repeating the previous steps. Therefore, the graphs get more detailed, which is one of the main properties of the "Evolving Function" as shown in Figures 13 and 14.
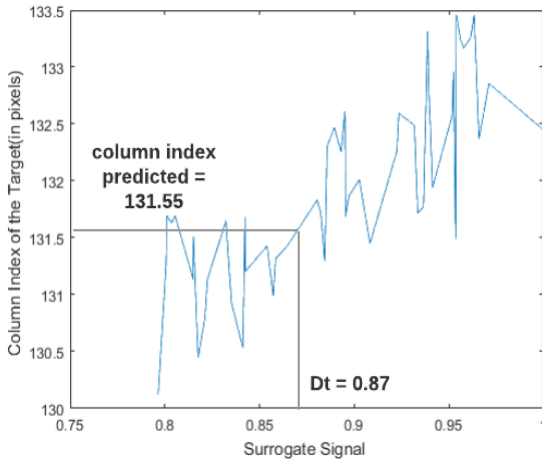
Figure 13: More detailed graph than that in Figure 11 as a result of more acquired data.
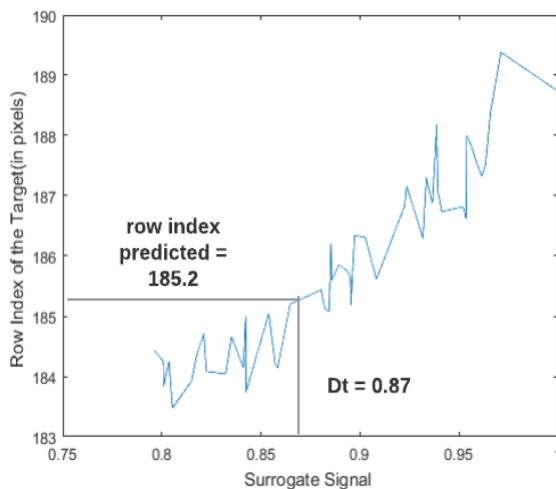

Figure 14: More detailed graph than that in Figure 12 as a result of more acquired data.

If a new surrogate signal is acquired, it is combined with n-1 surrogate signals before it to form a set D_t. The degree of closeness between D_t and D_{ref} is calculated and used to predict the position of the target at the same frequency of the surrogate signal as shown in Figures 13 and 14. The advantage of this newly introduced algorithm is that if an exact non-linear mathematical function exists between targets in the MR image and the surrogate signal, this is concluded by keeping reliable points and connecting them. So, as more points are obtained, the curve gets more detailed and closer to the real non-linear relation. If only a strong correlation between targets in the MR image

and the surrogate signal and not an exact function, also this algorithm captures it. That is because only points so close to the straight line capturing the correlation are preserved. Moreover, connecting by straight lines between reliable acquired points leads to that any predicted position of the target will be an average of two reliable acquired positions of the target. These two positions correspond to the two closest sets of surrogate signals D_{T1} and D_{T2} to the new set D_t.

C. Experiments
The two newly introduced approaches in this study were tested using:
- Open source data provided by [7].
- Experiments carried out previously by our research group and presented in [15].
- Experiments carried out on a phantom outside MR.

C.1 Open Source Data
Open source data is provided by Preiswerk et al. in [7]. It represents experiments carried out on humans. These experiments were MR images of the liver acquired simultaneously with ultrasound data using a single transducer. The acquisition of ultrasound data was triggered by the repetition cycle TR. The experiments setup was as follows:
- The employed MR system was 3 Tesla. Experiments were implemented on a "GE Signa HDxt" (40 mT/m, 150 T/m/s) system (Milwaukee, Wisconsin, USA) as well as a "Siemens Verio" system (45 mT/m, 200 T/m/s) (Erlangen, Germany).
- A single element transducer (Imasonics, Voray-sur-l'Ognon, France, 8-mmdiameter, 5 MHz, impedance matching layer of 1.5MRayl), which is small enough to fit below or within the openings of a multi-element MR receiver coil(GE 8-channel cardiac array, or Siemens body matrix).
- To achieve high accuracy, the transducer was positioned so that its beam passed near the center of the region of interest.
- The field of the OCM sensor wasn't focused. It penetrated and reflected multiple times within the region of intereset.
- The transducer was inserted into a rubber disc with diameter 3.5cm and thickness 1.4cm.
- Fiber-optic temperature probes (Neoptix ReFlex, Qualitrol Company, Fairport, New York, USA) were used to detect potential heating of the transducer for safety.

- The front and the back of the transducer were coated with ultrasound gel for proper coupling with the skin and optical fibers.
- The transducer and the optical fibers were fixed on the abdomen of the patient using adhesive bandage. Also, the coaxial cable of the transducer was covered by blue sheath of foam to insulate it thermally from the patient.
- An Olympus 5072PR pulser receiver (Olympus Scientific Solutions Americas, Waltham, Massachusetts, USA) was used to control the transducer and it was triggered by MR pulse sequence.
- A PCI digitizer card NI 5122, 150 MHz, 200 MS/s, 12-bit, 512 MB (National Instruments, Austin, Texas) was used for analog to digital conversion of the ultrasound data.

Data was acquired in eight imaging sessions. These experiments were carried out on seven volunteers, where one of them was imaged twice on different days. These experiments were labeled from A to H. In every imaging session, two planes of the liver were imaged. These planes were sagittal and coronal. The open source data is found in this link: https://github.com/fpreiswerk /OCMDemo. It contains sample data of sessions A, B and H. The data used to test the two algorithms presented in this paper was the data of coronal plane in session A only. The parameters of used images for testing the algorithms are as follows: number of images (Nt) is 92 images, N_Y is 192, N_{echoes} is 2, TR is 18 ms, R is 3.0 and the time required for one image acquisition is 0.576 s, slice thickness 5 mm, flip angle is 30°, matrix size is 192 x 192, field of view is 38 x 38 cm^2, number of repetition cycles is 32.

C.2 Previous Experiment

Also, the two newly developed algorithms were assessed using experiments carried out by our research group previously and presented in [15]. In these experiments, MR images of the liver were obtained simultaneously with the images of skin markers. The position of skin markers was used as the surrogate signal. The speed of MRI acquisition was 1 frame per second, while that of skin markers acquisition was 10 frames per second. The setup of experiments was as follows:

- 0.25 T open-bore MRI system. This system was the "ESAOTEc G-scan Brio system (Genoa, Italy)" installed at the university of Twente.
- Two 3D printed skin markers, each with a diameter of 2 cm. The markers were fixed on the abdomen 5 cm apart from each other and away from the MR coil.
- An industrial camera was used to track the skin markers. This camera was "MVBlueFox3" from

Matrix Visionc (Oppenweiler, Germany). It was placed 2 meters away from the center of the MR bore.

Data was acquired from 6 imaging sessions on 3 volunteers, one female and two males. Each subject was subjected to two imaging session, each for 3 minutes. MR images were acquired only for the sagittal plane. The properties of acquired MR images are as follows: slice thickness is 15 mm, repetition time is 7 s, echo time is 3.5 s, flip angle is 40° and field of view is 38 mm x 38 mm. The two newly developed algorithms were tested using the data of the first session of the first volunteer only. The video of skin markers of the first session of the first volunteer was re-processed in this paper. That's because the surrogate signal used here is the x-y pixel co-ordinates of the center of each skin marker in each frame of the video, not their relative positions to the reference frame as was used in [15]. The center of each marker was tracked between frames using Hough transform for detecting circles. Each image acquisition corresponds to the acquisition of 10 readings of the surrogate signal. Since, the acquisition of the surrogate signal was not triggered by the repetition time TR in these experiments. Therefore, the data had to be adapted to be suitable for the first algorithm presented by this study. Hence, the k space lines of each MR image were divided into 10 sections, where each section was time-matched with the acquisition of one reading of the surrogate signal.

C.3 Phantom Experiment

The "Evolving Function" algorithm was also tested by carrying out an experiment on a phantom that mimics the human liver. Surrogate signals used were skin markers and ultrasound. The readings of both surrogate signals were acquired simultaneously to evaluate whether it is important to use a precise surrogate with a complex and expensive setup like ultrasound or it is just sufficient to use a cheap one with less correlation to the target motion like skin markers to get results with accepted accuracy. As experiments were carried outside MR, the real position of a specific target inside the liver mold was obtained using an electromagnetic (EM) tracker. The experiment setup was as follows:

- Liver mold was prepared by mixing 120 g gelatin with 1200 cc of water.
- NDI medical aurora EM tracker was inserted inside the liver mold as shown in Figure 15.
- Liver mold was fixed on a plastic sheet as shown in Figure 15, which was allowed to move back and forth in both AP and SI directions by applying air pressure and vacuuming it. Two SI actuators and one AP actuator were used.
- Pressure applied for AP actuator was around 2

bar, while that applied for SI actuators was < 1 bar.

- Maximum displacement in the SI direction was 35 mm, while in AP direction 10 mm.
- Three solenoid valves were used. A valve for each actuator. Each valve had two inputs. One input was connected to air flow coming from air compressor while the other was connected to vacuum pump. The output of the valve went into the actuator.
- Switching the valves on and off was controlled using Arduino UNO board.
- Latex sheet of thickness 0.38 mm was used to mimic skin.
- Three plastic markers were fixed on the latex sheet. The markers were tracked using Logitech c920 hd pro camera.
- The ultrasound setup was as follows: a single element 5 MHz unfocused transducer, 5077 PR Olympus pulser receiver that triggered the transducer at a frequency of 100 Hz and an oscilloscope.
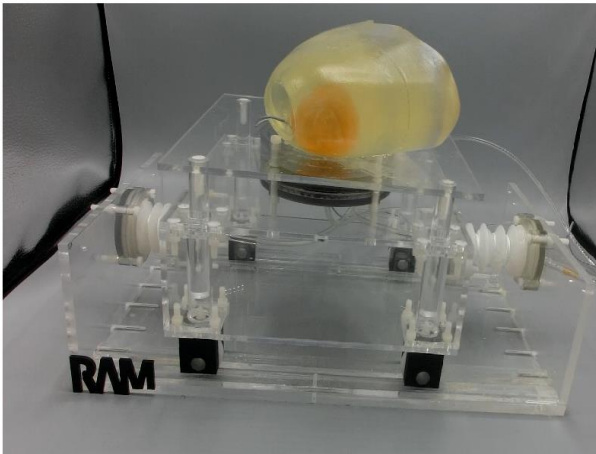

Figure 15: Phantom experiment. The orange part in the mold is the target tracked by the EM tracker, which is inserted inside it.

D. Validation

This subsection explains the methods used for quantitative and qualitative validation of the previously introduced two algorithms.

D.1 New Approach for Synthetic MRI Generation

The algorithm introduced for generating synthetic high frame rate MRI with spatial resolution and contrast better than real acquired images was evaluated regarding two aspects: the correctness of the algorithm and the quality of images generated by this algorithm regarding contrast and spatial resolution.

D.1.1 Correctness Validation

The correctness of the algorithm measures how close the positions of structures in synthetic images like: lesions, blood vessels and contour of the liver are to their real positions. Acquired MR images were used as the golden reference, indicating the real position of structures. Synthetic images, generated at the acquisition of surrogate signal corresponding to the acquisition of the k space centers of the corresponding acquired images, were used for the evaluation of the correctness of the algorithm by comparing them to their corresponding acquired ones. Correctness of the algorithm was evaluated by three methods:

- Tracking the centroid of a blood vessel in MR images.
- Tracking all surf features in the liver and structures surrounding it in MR images.

Firstly, the position of the centroid of a blood vessel in the open source data, which looks like a lesion, was tracked between each acquired MR image and the corresponding synthetic one as shown in Figure 16. The centroid was detected by detecting minimum eigenvalue feature in the region where this blood vessel exists in each acquired image and tracking its position in corresponding synthetic ones. The error between each acquired image and corresponding synthetic one was calculated as the Euclidian distance between the position of the centroid in each image. The total error was calculated as the average of all errors resulting from comparing synthetic images to their corresponding acquired ones.
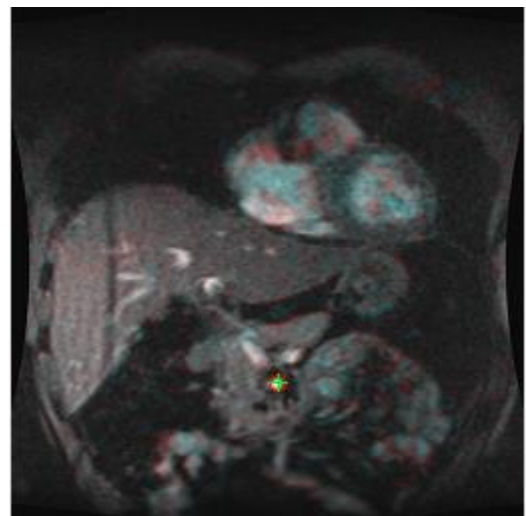

Figure 16: Tracking the centroid of blood vessel between each acquired image and the corresponding synthetic one. The red marker refers to the position of the centroid in the acquired image, while the green one refers to its position in the corresponding synthetic image.

Secondly, all SURF features in the liver and structures surrounding it in MR images were tracked between each acquired image and the corresponding synthetic one as shown in Figure 17. SURF features were chosen as they are so fast to compute and they have the same high performance as SIFT features [26] [27]. Also, they are distributed over all the image not just focused in the center [28]. The error was calculated as the average of Euclidian distances between all surf features tracked between each acquired image and the corresponding synthetic one. The total error was calculated as the average of all errors resulting from comparing synthetic images to their corresponding acquired ones.
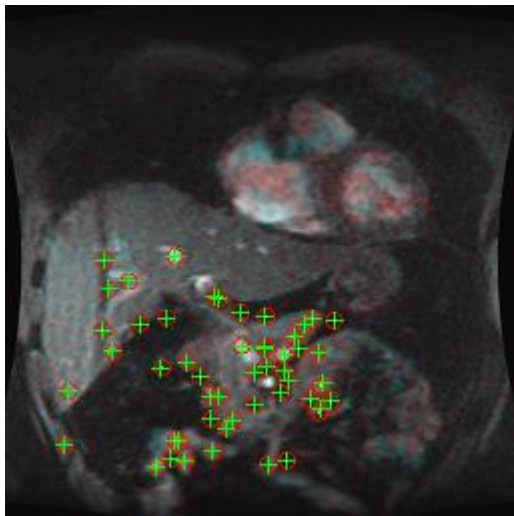

Figure 17: Tracking surf features in the liver and other structures between each acquired image and the corresponding synthetic one. The red markers refer to the positions of the SURF features in the acquired image, while the green ones refer to their positions in the corresponding synthetic image.

D.1.2 Quality Validation

The quality of synthetic images was evaluated by two metrics:
- Entropy
- BlurMetric, introduced in [1].

Entropy was introduced by Shanon in 1948 and it is a measure of image information content. The higher the value of entropy of an image, the more detailed information the image has and vice versa [25]. Entropy of a gray scale image is calculated as:

$$H = -\sum_{k=0}^{M-1} pk \, log2(pk) \qquad [8]$$

Where M is the number of gray levels and pk is the probability associated with each level. The minimum entropy happens for an image, where all pixels have the same level. Therefore, it could be concluded that images with high contrast have higher entropy and vice versa.

Comparing the contrast of synthetic images to their corresponding acquired ones was achieved by comparing the average entropy of all acquired images to the average entropy of the corresponding synthetic ones. Also, the histograms of both synthetic and corresponding acquired images were generated to visualize whether higher entropy values meant more information content or more noise. Histograms show the number of occurrences of the 256 gray levels in the image. If higher entropy means more information, then the histogram of the synthetic image should have more uniform distribution of the number of occurrences of the gray levels mainly forming the corresponding acquired image compared to the histogram of the acquired image. If higher entropy means noise, then this means that the number of occurrences of the gray levels mainly forming the corresponding acquired image doesn't get more uniform in the histogram of the synthetic image, however the histogram of the synthetic image introduces noise in other gray levels which didn't contribute to the formation of the real image. Figure 18 a shows an acquired image and its histogram, while Figure 18 b shows the corresponding synthetic image and its histogram.

The spatial resolution of the synthetic images was evaluated using the blur metric introduced in [1]. The blurriness of every image was given a value between [0,1], where 0 means a very sharp image and 1 means a very blurred one. The idea of the approach introduced in [1] is that blurriness means the loss of high frequency components and the more blurred the image is, the more the neighboring pixels converge to the same gray level. Therefore, if an image is very sharp and then it is blurred, there will be a very big difference between the sharp and the blurred versions. However, if the image is already blurred and then it is re-blurred, there won't be a very big difference between both of them. Therefore, the blurriness of an image is evaluated by this approach by blurring the image with a strong low pass filter and comparing the blurred version to the original version. If the original version was sharp, there would be a significant difference between both versions and vice versa. The spatial resolution of synthetic images was compared to their corresponding acquired ones by comparing the average blurriness of all acquired images and the average blurriness of all corresponding synthetic ones.

D.2 "Evolving Function" Machine Learning Algorithm

The evolving function introduced in subsection III B was validated regarding two aspects: correctness and the property of evolution. Correctness was measured by comparing the predicted x-y pixel co-ordinates of the

target, obtained as explained in Figures 16 and 17, to the real position of the target. The error was calculated as the Euclidian distance between the predicted position and the real one. The real position of a target is obtained by tracking a certain feature in all acquired images. The property of evolution was tested by training the evolving function with different portions of the acquired data and testing the average error of the model every time by the same fixed portion of data. If the average error improves when the data used for training increases, this means that the property of evolution of the model is preserved. Firstly, the model was created using only the first 50 % of the acquired images and tested with the last 25% of the acquired images. Afterwards, it was created using 75% of the acquired data and tested with the same 25% of the data used for verification in the previous step. The model was validated by repeating all the previous steps for more than a target. These targets were:

- The center of the blood vessel used for validation of the first algorithm.
- A chosen surf feature in the liver.

IV. RESULTS

The validation strategy introduced in subsection III D was applied to the: open source data, data obtained from previously carried out experiments by our group and data obtained from carried out experiments on the phantom. For open source data, some of the used images corresponded to coughing or gasping. These images were not omitted from testing to challenge the newly introduced algorithms.

A New Approach for Synthetic MRI Generation

A.1 Correctness Validation

The mean error for tracking the center of the blood vessel between all acquired images and their corresponding synthetic ones as shown in Figure 16 using the open source data was 0.659 pixel. The minimum error was 0.1035 pixel. The maximum error was 3.4592 pixels in case of coughing and the standard deviation was 0.6238 pixel. The mean error for tracking all surf features in the liver and neighboring structures between all acquired images and the corresponding synthetic ones as shown in Figure 17 using the open source data was 1.2154 pixels. The minimum error was 0.288 pixel. The maximum error was 6.0451 pixels in case of coughing and the standard deviation was 1.0635 pixel.

A.2 Quality Validation

The average entropy of acquired images using open source data was 6.5248, while that of the corresponding synthetic ones was 6.5631. Since, higher entropy in this case means more information not noise as could be inferred from Figure 18. Therefore, the newly introduced algorithm results in synthetic images with contrast better than the real acquired ones using MR. The minimum entropy of the synthetic images was 6.3076. The maximum entropy was 6.8566 and the standard deviation was 0.1106. The average blurriness of acquired images using open source data was 0.3306, while that of corresponding synthetic ones was 0.3305. Therefore, the newly introduced algorithm results in synthetic images with higher spatial resolution than the real acquired ones. The minimum blurriness of the synthetic images was 0.321. The maximum blurriness was 0.3416 and the standard deviation was 0.0047. The results are summarized in Table 1. On the other hand, the limitation of the newly introduced algorithm for generating high frame rate MRI in this paper is that the surrogate signal should be obtained at very high frequency, almost every repetition cycle *TR*. Otherwise, the resulting images will be of a poor quality compared to the acquired ones as it was the case using the data obtained from previous carried out experiments by our research group using skin markers as shown in Figure 19. In these experiments, the frequency of the surrogate signal was only 10 times higher than that of MR acquisition, while in the experiments of the open source data the frequency of the surrogate signal was 32 times higher than MR acquisition.

Comparison Aspect	Mean Value	Min. Value	Max. Value	Standard Deviation
Error in tracking the center of a blood vessel	0.659 pixel	0.1035 pixel	3.4592 pixels	0.6238 pixel
Error in tracking SURF features	1.2154 pixels	0.288 pixel	6.0451 pixels	1.0635 pixels
Entropy	6.5631	6.3076	6.8566	0.1106
Blurriness	0.3305	0.321	0.3416	0.0047

Table 1: Summary of the results of the new approach for synthetic MRI generation.
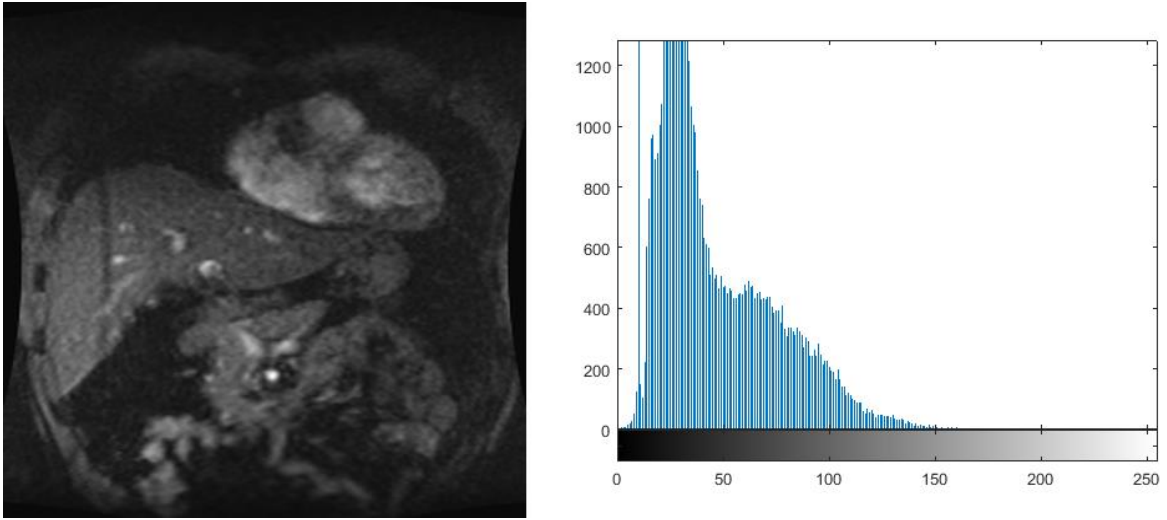
(a)
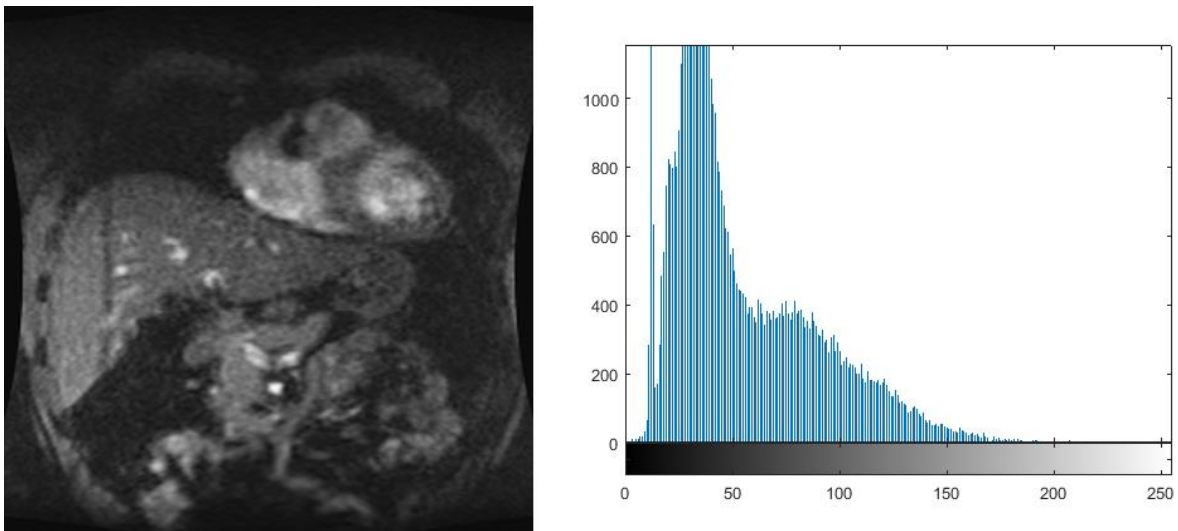
(b)

Figure 18: Acquired MR image and its corresponding histogram, showing the number of occurrences of each gray level forming the image (a). Synthetic MR image corresponding to the acquired image showed in (a) and its histogram (b).
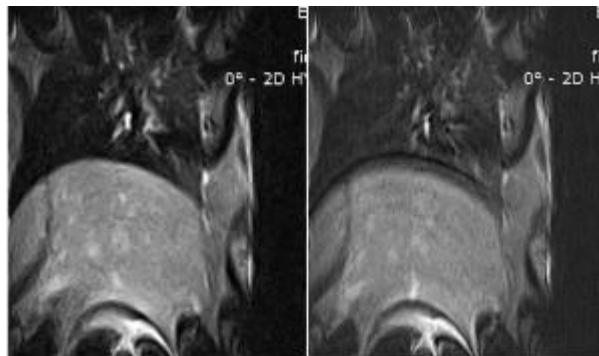

Figure 19: The left MR image is the acquired one, while the one to the right is the corresponding synthetic one.

B. "Evolving Function" *Machine Learning Algorithm*

The mean error for estimating the center of the blood vessel using the open source data and after training the evolving function by 50% of the data and testing it by the last 25% of the data was 1.0034 pixels. The minimum error was 0.196 pixel. The maximum error was 1.6857 pixels and the standard deviation was 0.3639 pixel. The mean error after training the evolving function by 75% of the acquired data presented in the open source decreased to 0.8669 pixel. The minimum error was 0.1535 pixel. The maximum error was 1.6435 pixels and the standard deviation was 0.4156 pixel. The mean error for estimating the position of one of the surf points in the liver using the open source data after training the evolving function by 50% of the acquired data was 0.9859 pixel. The minimum error was 0.3884 pixel. The maximum error was 1.9863 pixels and the standard deviation was 0.3534 pixel. The mean error decreased to 0.8758 pixel after training the algorithm by 75% of the data. The minimum error was 0.2022 pixel. The maximum error was 1.8091 pixels and the standard deviation was 0.3995 pixel.

On the other hand, the main limitation of this algorithm is that acquired MR images should have good spatial resolution and contrast. Otherwise, the tracker used to detect the real position of the target in acquired images won't be precise. This will result into training the algorithm with inaccurate data as it was the case using the data obtained from previous experiments carried by our group, where the mean error of the evolving function was around 2 pixels.

The mean error for estimating the position of a target in the phantom, using skin markers as a surrogate signal, was 2.79 mm after training the algorithm by 50% of the data. The mean error decreased to 2.75 mm after training the algorithm by 75% of the data. This proves that cheap surrogate signals with less correlation to the liver motion like skin markers could be used to achieve high accuracy. The mean error for estimating the position of a target in the phantom, using ultrasound as a surrogate signal, was 8.5 mm after training the algorithm by 75% of the data. That was because the obtained ultrasound readings were so noisy due to some limitations in the experiment setup. The results are summarized in Table 2.

V. CONCLUSION

This study introduces two techniques for overcoming the problem of low frequency MR imaging during percutaneous minimally invasive procedures in the liver, which hinders real-time tracking of targets. Both techniques presented by this study depend on the passive approach of respiratory motion compensation using a surrogate signal. The first technique enables generating synthetic images at the same high frequency of the surrogate signal. Hence, enabling real-time tracking of

Comparison Aspect	Mean Value 50%	Mean Value 75%
Error in predicting the center of a blood vessel	1.0034 pixels (2.1 mm)	0.8669 pixel
Error in predicting the Position of a SURF feature in the liver	0.9859 pixel	0.8758 pixel
Error in predicting the position of a target in the phantom	2.79 mm	2.75 mm

Table 2: Summary of the results of the "Evolving Function". "Mean 50%": refers to the mean value of the error after training the algorithm by 50% of the data. "Mean 75%": refers to the mean value of the error after training the algorithm by 75% of the data.

targets. Moreover, the contrast and spatial resolution of the synthetic images are higher than that of acquired ones. This enables better targeting for small and critical targets in the liver with very high accuracy. The correctness of that technique was measured by comparing the locations of liver features in synthetic images to their corresponding acquired ones. The mean error ranged between 0.659 to 1.2154 pixels. The second technique, named "Evolving Function", enables predicting the pixel co-ordinates of a certain target at the same high frequency of surrogate signal acquisition without generating full synthetic images. The strength of this technique is that it concludes the exact non-linear relation between the surrogate signal and the target if it exists. If no exact function exists, it captures the correlation between them as close as possible. As more data is provided, the non-linear function modelling the relation between the surrogate signal and the target improves to capture the relation between them more precisely. Therefore, this technique allows high accuracy in estimating the location of very small targets in real-time. The correctness of the technique was measured by comparing the predicted positions of some targets to their real positions. The mean error after training the algorithm by 50% of the acquired data ranged between 0.9859 to 1.0034 pixels. The mean error decreased after training the algorithm by 75% of the data to range between 0.8669 to 0.8758 pixel.

On the other hand, there exists some limitations for these techniques. The limitation of the first technique is that the frequency of the surrogate signal should be so high. Otherwise, the quality of the synthetic images drops so much. The limitation of the second technique is that MR images used for training should have very high spatial resolution and contrast. Otherwise, the positions of the target used as golden references for training the algorithm will be unreliable. This in turn results in an unreliable model that generates inaccurate predictions.

Also, this study proves that it is not essential to use a surrogate signal with a complex and expensive setup like ultrasound and it is just sufficient to use a cheap one with less correlation to the target motion like skin markers to get results with accepted accuracy. That was proved by carried out experiment on a phantom, where the mean error in estimating the position of a target using skin markers as a surrogate and "Evolving Function" as the learning algorithm was 2.75 mm.

References

[1] F. Crete-Roffet, T. Dolmiere, P. Ladret, M. Nicolas, "The Blur Effect: Perception and Estimation with a New No-Reference Perceptual Blur Metric", Proceedings of SPIE – The International Society For Optical Engineering, March 2007.

[2] "Cijfers over kanker, nederlandse kankerregistratie," accessed August 2017. [Online]. Available: http://www.cijfersoverkanker.nl/.

[3] "World health organization, cancer key facts," Feb 2017, accessed August 2017. [Online]. Available: http://www.who.int/mediacentre/factsheets/fs297/en/.

[4] M. Abayazid, T. Kato, S. G. Silverman, and N. Hata, "Using needle orientation sensing as surrogate signal for respiratory motion estimation in percutaneous interventions," International Journal of Computer Assisted Radiology and Surgery, 2017.

[5] M. A. Clifford, F. Banovac, E. Levy, and K. Cleary, "Assessment of hepatic motion secondary to respiration for computer assisted interventions," Computer Aided Surgery, vol. 7, no. 5, pp. 291–299, 2002.

[6] B. Stemkens, R. H. Tijssen, B. D. de Senneville, H. D. Heerkens, M. van Vulpen, J. J. Lagendijk, and C. A. van den Berg, "Optimizing 4-dimensional magnetic resonance imaging data sampling for respiratory motion analysis of pancreatic tumors," International Journal of Radiation Oncology* Biology* Physics, vol. 91, no. 3, pp.571–578, 2015.

[7] F. Preiswerk, M. Toews, C.-C. Cheng, y. G. Chiou Jr, C.-S. Mei, L. F. Schaefer, W. S. Hoge, B. M. Schwartz, L. P. Panych, and B. Madore, "Hybrid mri-ultrasound acquisitions, and scannerless real-time imaging," Magnetic resonance in medicine, 2017.

[8] Alterovitz R, Pouliot J, Taschereau R, Hsu ICJ, Goldberg K (2003) Simulating needle insertion and radioactive seed implantation for prostate brachytherapy. In: Westwood JD, Hoffman HM, Mogel GT, Phillips R, Robb RA, Stredney D (eds) Studies in health technology and informatics, vol 94. IOS Press, pp 19–25.

[9] Bell MAL, Byram BC, Harris EJ, Evans PM, Bamber JC (2012) In vivo liver tracking with a high volume rate 4d ultrasound scanner and a 2d matrix array probe. Phys Med Biol 57(5):1359

[10] K. Langen and D. Jones, "Organ motion and its management," International Journal of Radiation Oncology* Biology* Physics, vol. 50, no. 1, pp. 265–278, 2001.

[11] S. Shimizu, H. Shirato, B. Xo, K. Kagei, T. Nishioka, S. Hashimoto,K. Tsuchiya, H. Aoyama, and K. Miyasaka, "Three-dimensional movement of a liver tumor detected by high-speed magnetic resonance imaging," Radiotherapy and oncology, vol. 50, no. 3, pp.367–370,1999.

[12] K. E. Barrett et al., "Ganong's review of medical physiology," 2010.

[13] P. J. Keall, G. S. Mageras, J. M. Balter, R. S. Emery, K. M. Forster, S. B. Jiang, J. M. Kapatoes, D. A. Low, M. J. Murphy, B. R. Murray et al., "The management of respiratory motion in radiation oncology report of aapm task group 76," Medical physics, vol. 33, no. 10, pp.3874–3900, 2006.

[14] Zhou Y, Thiruvalluvan K, Krzeminski L, MooreWH, Xu Z, Liang Z (2013) Ct-guided robotic needle biopsy of lung nodules with respiratory motion experimental system and preliminary test. Int J Med Robot Comput Assist Surg 9(3):317–330

[15] S. Fahmi, F. Simonis, M. Abayazid, "Respiratory Motion Estimation of the Liver with Abdominal Motion as a Surrogate: A Supervised Learning Approach", The International Journal of Medical Robotics and Computer Assisted Surgery, 2018.

[16] Suramo I, Paivansalo M, Myllyla V. Cranio-caudal movements of the liver, pancreas and kidneys in respiration. Acta Radiol Diagn 1984;25:129–131.

[17] McClelland JR (2013) Estimating internal respiratory motion from respiratory surrogate signals using correspondence models, chap.9. Springer, Berlin, pp 187–213.

[18] F. Ernst, V. Martens, S. Schlichting, A. Beˇsireviˊc, M. Kleemann,C. Koch, D. Petersen, and A. Schweikard, "Correlating chest surface motion to motion of the liver using "-svr–a porcine study," Medical Image Computing and Computer-Assisted Intervention–MICCAI 2009, pp. 356–364, 2009.

[19] A. S. Beddar, K. Kainz, T. M. Briere, Y. Tsunashima, T. Pan, K. Prado, R. Mohan, M. Gillin, and S. Krishnan, "Correlation between internal fiducial tumor motion and external marker motion for liver tumors imaged with 4d-ct," International Journal of Radiation Oncology* Biology* Physics, vol. 67, no. 2, pp. 630–638, 2007.

[20] J. D. Hoisak, K. E. Sixel, R. Tirona, P. C. Cheung, and J.-P. Pignol, "Correlation of lung tumor motion with external surrogate indicators of respiration," International Journal of Radiation Oncology* Biology* Physics, vol. 60, no. 4, pp. 1298–1306, 2004.

[21] R. D¨urichen, L. Davenport, R. Bruder, T. Wissel, A. Schweikard, and F. Ernst, "Evaluation of the potential of multi-modal sensors for respiratory motion prediction and correlation," in Engineering in Medicine and Biology Society (EMBC), 2013 35th Annual International Conference of the IEEE. IEEE, 2013, pp. 5678–5681.

[22] Shimizu S, Shirato H, Aoyama H, Hashimoto S, Nishioka T, Yamazaki A, Kagei K, Miyasaka K. Highspeed magnetic resonance imaging for four-dimensional treatment planning of conformal radiotherapy of moving body tumors. Int J Radiat Oncol Biol Phys 2000;48:471–474.

[23] P. Sprawls, "Magnetic Resonance Imaging", Medical Physics Publishing, 2000.

[24] Pavlicek W. MR instrumentation and image formation. RadioGraphics 1987; 7(4):809-814.

[25] Tsai, D. Y., Lee, Y., and Matsuyama, E. Information entropy measure for evaluation of image quality. Journal of Digital Imaging, 21, 3 (Sep. 2008), 338–347.

[26] P M Panchal, S R Panchal, S K Shaj, "A Comparison of SIFT and

SURF", International Journal of Innovative, Research in Computer and Communication Engineering, vol.1, Issue 2, April 2013.

[27] L. Juan, O. Gwun, " A Comparison of SIFT, PCA-SIFT and SURF", IJIP, vol.3(4), 2009.

[28] E.Karami, S.Prasad, M.Shehata, "Image Matching using SIFT, SURF, BRIEF and ORB: Performance Comparison for Distorted Images", in Proceedings of the 2015 Newfoundland Electrical and Computer Engineering Conference, St. John's, Canada, November, 2015.